Studies of granularity of a hadronic calorimeter for tens-of-TeV jets at a 100 TeV pp collider

C.-H. Yeh[a], S.V. Chekanov[b], A.V. Kotwal[c,d], J. Proudfoot[b], S. Sen[c], N.V. Tran[d], S.-S. Yu[a]

[a] *Department of Physics, National Central University, Chung-Li, Taoyuan City 32001, Taiwan*
[b] *HEP Division, Argonne National Laboratory, 9700 S. Cass Avenue, Argonne, IL 60439, USA.*
[c] *Department of Physics, Duke University, USA*
[d] *Fermi National Accelerator Laboratory*
[e] *Department of Physics, Michigan State University, 220 Trowbridge Road, East Lansing, MI 48824*

Abstract

Jet substructure variables for hadronic jets with transverse momenta in the range from 2.5 TeV to 20 TeV were studied using several designs for spacial size of calorimeter cells. The studies used the full Geant4 simulation of calorimeter response combined with realistic reconstruction of calorimeter clusters. In most cases considered in this study the results indicate that the performance of jet-substructure reconstruction improves with reducing cell sizes of a hadronic calorimeter from $\Delta\eta \times \Delta\phi = 0.1 \times 0.1$ to 0.022×0.022.

Keywords: multi-TeV physics, pp collider, future hadron colliders, FCC, SppC

1. Introduction

Particle collisions at energies beyond those attained at the LHC will lead to many challenges for detector technologies. Future experiments, such as high-energy LHC (HE-LHC), future circular pp colliders of the European initiative, FCC-hh [1] and the Chinese initiative, SppC [2] will be required to measure high-momentum bosons (W, Z, H) and top quarks with strongly collimated decay products that form jets. Studies of jet substructure can help identify such particles.

The reconstruction of jet substructure variables for collimated jets with transverse momentum above 10 TeV requires an appropriate detector design. The most important for reconstruction of such jets are tracking and calorimeter. Recently, a number of studies [3, 4, 5] have been discussed using various fast simulation tools, such as Delphes [6], in which momenta of particles are smeared to mimic detector response.

A major step towards the usage of full Geant4 simulation to verify the granularity requirements for calorimeters was made in [7]. The studies included in this paper have illustrated a significant impact of granularity of electromagnetic (ECAL) and hadronic

Email addresses: `jwzuzelski18@gmail.com` (C.-H. Yeh), `chekanov@anl.gov` (S.V. Chekanov), `ashutosh.kotwal@duke.edu` (A.V. Kotwal), `proudfoot@anl.gov` (J. Proudfoot), `sourav.sen@duke.edu` (S. Sen), `ntran@fnal.gov` (N.V. Tran), `syu@cern.ch` (S.-S. Yu)

(HCAL) calorimeters on the shape of hadronic showers calculated using calorimeter hits for two particles separated by some angle. It was concluded that high granularity is essential in resolving two close-by particles for energies above 100 GeV.

This paper makes another step in understanding of this problem in terms of high-level physics quantities typically used in physics analyses. Similar to the studies presented in [7], this paper is based on a full Geant4 simulation with realistic jet reconstruction.

2. Simulation of detector response

The description of the detector and software used for this study is discussed in [7]. We use the SiFCC detector geometry with a software package that represents a versatile environment for simulations of detector performance, testing new technology options, an event reconstruction techniques for future 100 TeV colliders.

The baseline detector discussed in [7] uses a steel-scintillator hadronic calorimeter with a transverse cell size of 5×5 cm^2, which corresponds to $\Delta\eta \times \Delta\phi = 0.022 \times 0.022$, where η is the pseudorapidity, $\eta \equiv -\ln\tan(\theta/2)$, and ϕ is the azimuthal angle. The depth of the HCAL in the barrel region is about 11.25 interaction lengths (λ_I). The HCAL has 64 longitudinal layers in the barrel and the endcap regions.

In addition, to the baseline HCAL geometry, several geometry variations were considered. We used the HCAL with the cells that have the transverse size of 20×20 cm^2, 2×2 cm^2 and 1×1 cm^2. In the terms of $\Delta\eta \times \Delta\phi$, such cell sizes correspond to 0.1×0.1, 0.01×0.01 and 0.005×0.005, respectively.

The GEANT4 (version 10.3) [8] simulation of calorimeter response was complemented with the full reconstruction of calorimeter clusters formed by the Pandora algorithm [9, 10]. Calorimeter clusters were built from calorimeter hits in the ECAL and HCAL after applying the corresponding sampling fractions. No other corrections are applied. Hadronic jets were reconstructed with the FastJet package [11] using the anti-k_T algorithm [12] with a distance parameter of 0.5.

In the following discussion, we use the simulations of a heavy Z' boson, a hypothetical gauge boson that arises from extensions of the electroweak symmetry of the Standard Model. The Z' bosons were simulated with the masses, $M = 5$, 10, 20 and 40 TeV. The lowest value represents a typical mass that is within the reach of the LHC experiments. The value 40 TeV represents the physics reach for a 100 TeV collider. The Z' particles are forced to decay to two light-flavor jets ($q\bar{q}$), W^+W^- or $t\bar{t}$, where W and t decay hadronically. In all such scenarios, two highly boosted jets are produced, which are typically back-to-back in the laboratory frame. Typical transverse momenta of such jets are $\simeq M/2$. The main difference between considered decay types lays in different jet substructure. In the case of the $q\bar{q}$ decays, jets do not have any internal structure. In the case of W^+W^-, each jet originates from W, thus it has two subjects because of the decay $W \to q\bar{q}$. In the case of hadronic top decays, jets have three subjects due to the decay $t \to W^+ b \to q\bar{q}b$. The signal events were generated using the Pythia8 generator with the default settings, ignoring interference with SM processes. The event samples used in this paper are available from the HepSim database [13].

3. Studies of jet properties

First let us consider several variables that represent jet substructure using different types of calorimeter granularity. The question we want to answer is how close the reconstructed jet substructure variables reflect the input "truth" values that are reconstructed using input particles directly from the PYTHIA8 generator.

In this study we use the jet effective radius and jet splitting scales as benchmark variables to study jet substructure properties for different calorimeter granularity scenarios. The effective radius is the average of the energy weighted radial distance δR_i in $\eta - \phi$ space of jet constituents. It is defined as $(1/E)\sum_i e_i \delta R_i$, where E is the energy of the jet and e_i is the energy of a calorimeter cluster i at the distance δR_i from the jet center. The sum runs over all constituents of the jet. Recently, it has been studied for multi-TeV jets in Ref.[14]. A jet k_T splitting scale [15] is defined as a distance measure used to form jets by the k_T recombination algorithm [16, 17]. This variable has been studied by ATLAS [18], and more recently in the context of 100 TeV physics [14]. The splitting scale is defined as $\sqrt{d_{12}} = \min(p_T^1, p_T^2) \times \delta R_{12}$ [18] at the final stage of the k_T clustering, where two subjets are merged into the final one.

Figures 1 and 2 show the distributions of the jet effective radius and jet splitting scale for different jet transverse momenta and HCAL granularities. The reconstructed-level distributions significantly disagree with the distributions reconstructed using truth-level particles. The distribution reconstructed with the cell sizes 1 $\times$1 cm^2 are closest to the truth-level variables. The distributions reconstructed using the cell size of 20 $\times$20 cm^2, show the largest discrepancy with the truth-level variables. Note that, in terms of closeness of reconstructed distributions to the truth level, there is no significant difference between 5 $\times$5 cm^2, 2 $\times$2 cm^2 and 1 $\times$1 cm^2 choices.

Thus this study confirms the baseline SiFCC detector geometry [7] that uses 5×5 cm^2 cells, corresponding to $\Delta\eta \times \Delta\phi = 0.022 \times 0.022$, Note that the ATLAS and CMS detectors use the HCAL cell sizes in the barrel region which are close to $\Delta\eta \times \Delta\phi = 0.1 \times 0.1$. According to this study, such HCAL cell sizes are not optimal in terms of performance for tens-of-TeV jets.

In the next few sections we will consider several other physics-motivated variables that can shed light upon the performance of the HCAL for tens-of-TeV jets.

4. Study of detector performance with soft drop mass

In this section, we use the jet mass computed with a specific algorithm, soft drop declustering, to study the performance of detector with various detector cell sizes and center-of-mass (c.m.) energies.

4.1. The technique of soft drop declustering

The soft drop declustering [19] is a grooming method that removes soft wide-angle radiation from a jet. The constituents of a jet j_0 are first reclustered using the Cambridge-Aachen (C/A) algorithm [20, 21]. Then, the jet j_0 is broken into two subjets j_1 and j_2 by undoing the last stage of C/A clustering. If the subjets pass the following soft drop condition, jet j_0 is the final soft-drop jet. Otherwise, the algorithm redefines j_0 to be the subjet with larger p_T (among j_1 and j_2) and iterates the

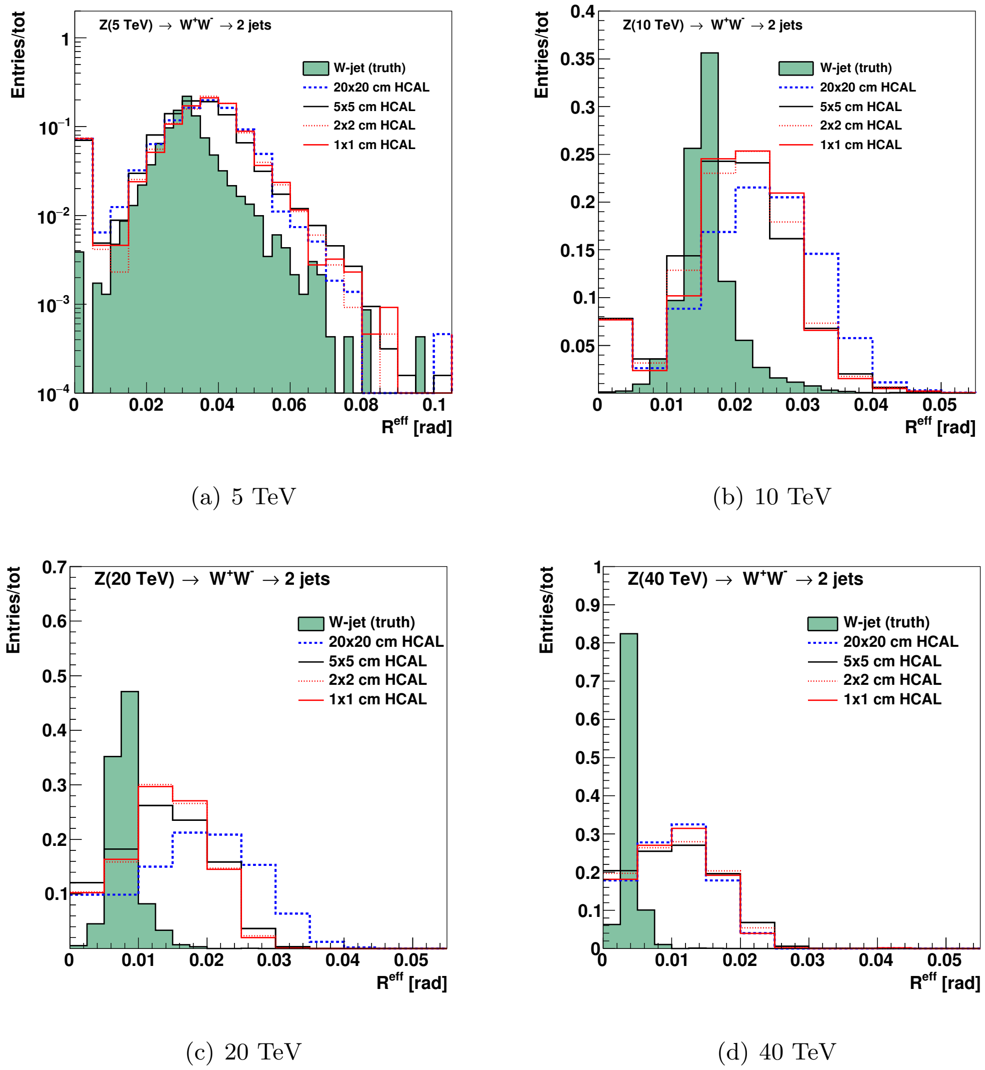

(a) 5 TeV

(b) 10 TeV

(c) 20 TeV

(d) 40 TeV

Figure 1: Jet effective radius for different jet transverse momenta and HCAL granularities.

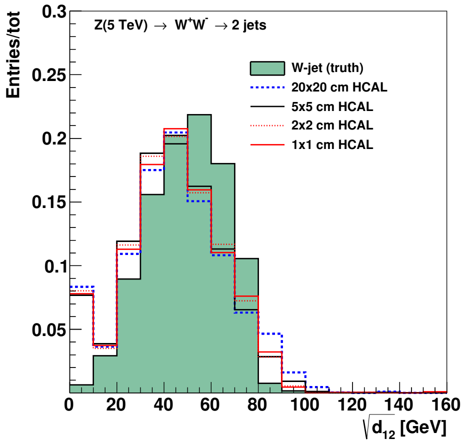

(a) 5 TeV

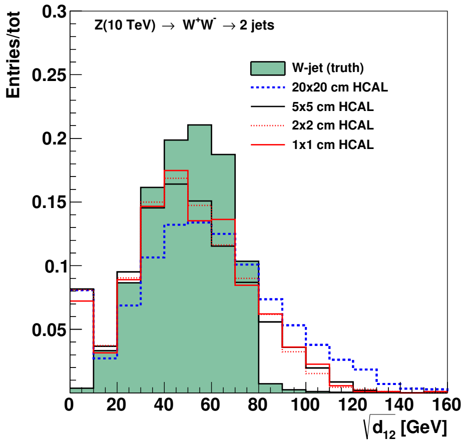

(b) 10 TeV

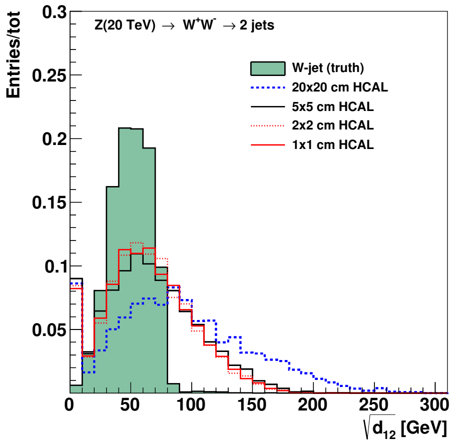

(c) 20 TeV

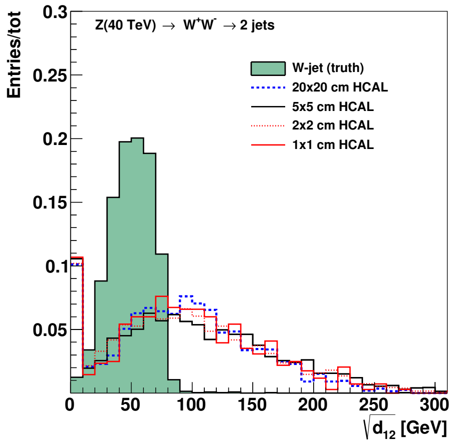

(d) 40 TeV

Figure 2: Jet splitting scale for different jet transverse momenta and HCAL granularity.

procedure.

$$\frac{\min(p_{T1}, p_{T2})}{p_{T1} + p_{T2}} > z_{\text{cut}}(\frac{\Delta R_{12}}{R_0})^{\beta}, \tag{1}$$

where p_{T1} and p_{T2} are the transverse momenta of the two subjets, z_{cut} is soft drop threshold, ΔR_{12} is the distance between the two subjets in the rapidity-azimuth angle plane (y-ϕ), R_0 is the characteristic radius of the original jet, and β is the angular exponent.

In our study, we compare the performance of a future detector when setting $\beta = 0$ versus when setting $\beta = 2$. For $\beta = 0$, the soft drop condition depends only on the z_{cut}. For $\beta = 2$, the condition depends on the angular distance between the two subjets and z_{cut} and the algorithm becomes infrared and collinear safe.

4.2. Analysis method

We employ the following method to quantify the detector performance and find out the cell size that gives the best separation power to distinguish signal from background. For each configuration of detector and c.m. energy, we draw the receiver operating characteristic (ROC) curves in which the x-axis is the signal efficiency (ϵ_{sig}) and y-axis is the inverse of background efficiency ($1/\epsilon_{\text{bkg}}$). In order to scan the efficiencies of soft drop mass cuts, we vary the mass window as follows. We first look for the median bin i_{med}[1] of the soft drop mass histogram from simulated signal events. Taking the right boundary of bin i_{med} as the center of mass window x_{center}, we start increasing the width of mass window symmetrically on the left and on the right of x_{center}, in steps of 5 GeV, i.e. the narrowest mass window is $[x_{\text{center}} - 5, x_{\text{center}} + 5]$. If one side reaches the boundary of the mass histogram, we only increase the width on the other side, also in steps of 5 GeV. For each mass window, there will be corresponding ϵ_{sig} and ϵ_{bkg}, which gives a point in the ROC curves.

4.3. Results and conclusion

Figures 3, 5, 7, and 9 show a few representative distributions for the soft drop mass for $\beta = 0$ and $\beta = 2$ with different c.m. energies and detector cell sizes; the signals considered are $Z' \to WW$ and $Z' \to t\bar{t}$.

Figures 4, 6, 8, and 10 show the ROC curves for different detector cell sizes and c.m. energies.

These studies show that the reconstruction of soft drop mass improves with decrease of the HCAL cell sizes. Figures 4 and 6 show that for $\beta = 0$ the smallest detector cell size, 1 cm $\times$ 1 cm, has the best separation power at $\sqrt{s}$ =5, 10, and 20 TeV when the signal is $Z' \to WW$ and at $\sqrt{s}$ =10 and 20 TeV when the signal is $Z' \to t\bar{t}$. On the contrary, Figs. 8 and 10 show that for $\beta = 2$ the smallest detector cell size does not have improvements in the separation power with respect to those with larger cell sizes. In fact, the performances of the three cell sizes are similar. In addition, sometimes bigger detector cell sizes, 5 cm $\times$ 5 cm or 20 cm $\times$ 20 cm have the best separation power.

We also find that the soft drop mass with $\beta = 0$ has better performance for distinguishing signal from background than for $\beta = 2$. Therefore, we will apply requirements on this variable when studying the other jet substructure variables.

[1] The integral from bin 0 to bin i_{med} ($i_{\text{med}} - 1$) should be greater (less) than half of the total number of events. Note, the bin width is 5 GeV.

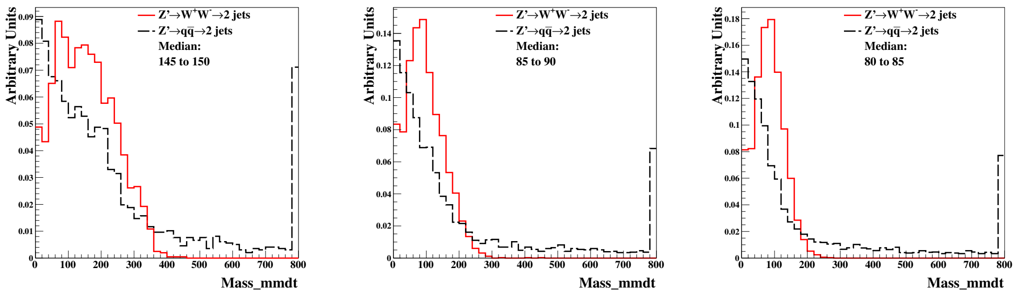

(a) 20×20(cm^2) (b) 5×5(cm^2) (c) 1×1(cm^2)

Figure 3: Distributions of soft drop mass for β=0, with 20 TeV c.m. energies and three different detector cell sizes: 20×20, 5×5, and 1×1 (cm^2). The signal (background) process is $Z' \to WW$ ($Z' \to q\bar{q}$).

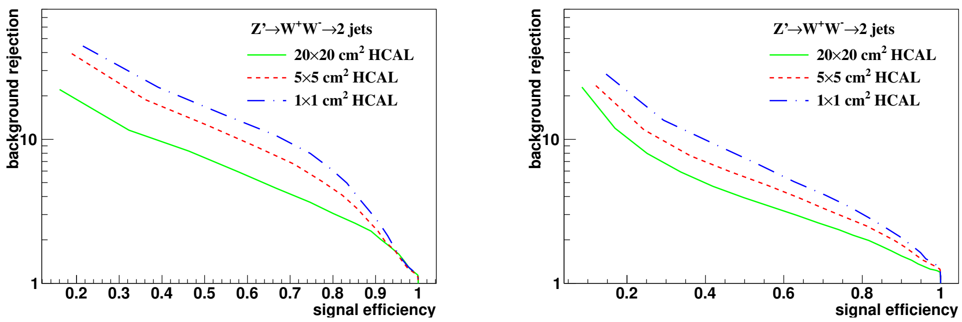

(a) Z'(5 TeV) (b) Z' (10 TeV)

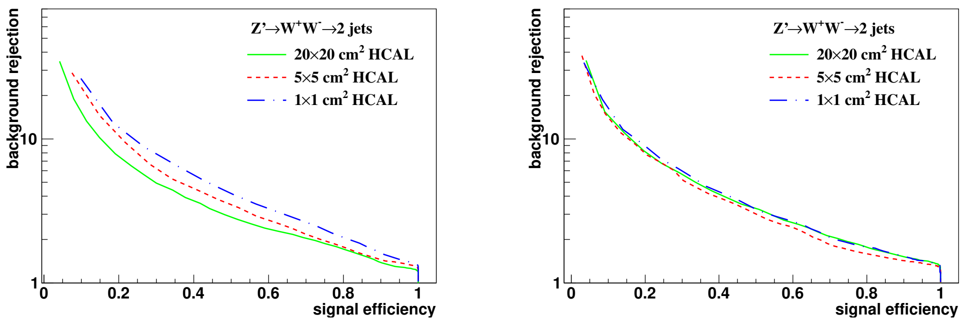

(c) Z' (20 TeV) (d) Z' (40 TeV)

Figure 4: The ROC curves of soft drop mass selection for β=0 with 5, 10, 20, 40 TeV c.m. energies. Three different detector cell sizes are compared: 20×20, 5×5, and 1×1 (cm^2). The signal (background) process is $Z' \to WW$ ($Z' \to q\bar{q}$).

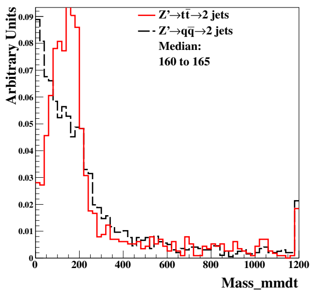

(a) 5×5 (cm^2)

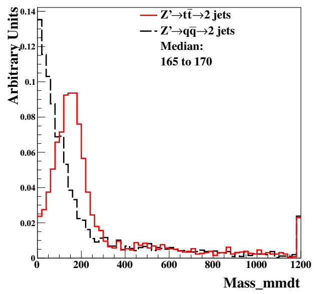

(b) 20×20 (cm^2)

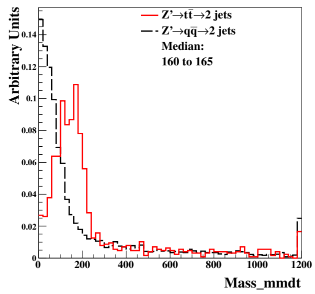

(c) 1×1 (cm^2)

Figure 5: Distributions of soft drop mass for β=0, with 20 TeV c.m. energies and three different detector cell sizes: 20×20, 5×5, and 1×1 (cm^2). The signal (background) process is $Z' \to t\bar{t}$ ($Z' \to q\bar{q}$).

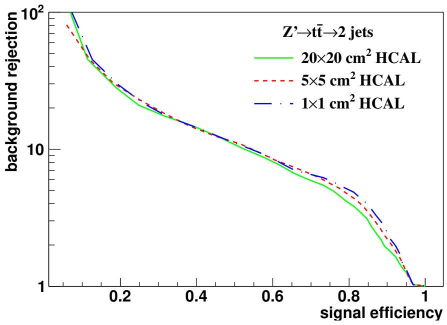

(a) Z' (5 TeV)

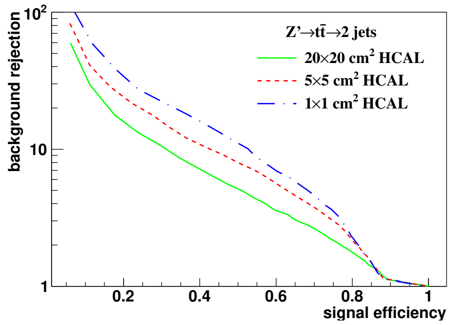

(b) Z' (10 TeV)

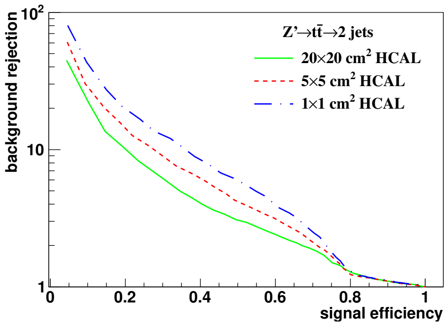

(c) Z' (20 TeV)

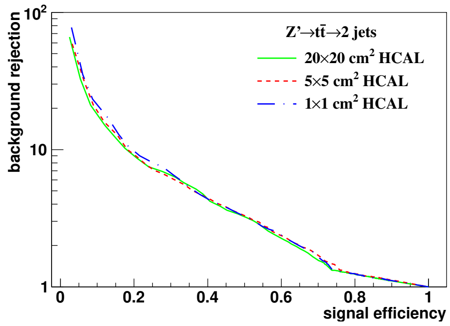

(d) Z' (40 TeV)

Figure 6: The ROC curves of soft drop mass selection for β=0 with 5,10, 20, 40 TeV c.m. energies. Three different detector cell sizes are compared: 20×20, 5×5, and 1×1 (cm^2). The signal (background) process is $Z' \to t\bar{t}$ ($Z' \to q\bar{q}$).

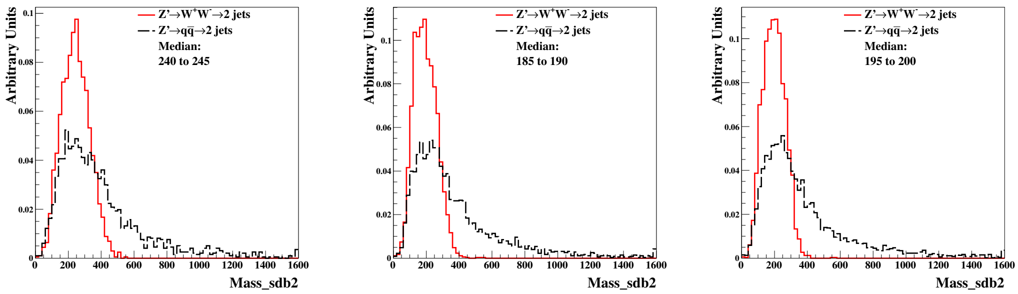

(a) 20×20 (cm^2) (b) 5×5 (cm^2) (c) 1×1 (cm^2)

Figure 7: Distributions of soft drop mass for β=2, with 20 TeV c.m. energies and three different detector cell sizes: 20×20, 5×5, and 1×1 (cm^2). The signal (background) process is $Z' \to WW$ ($Z' \to q\bar{q}$).

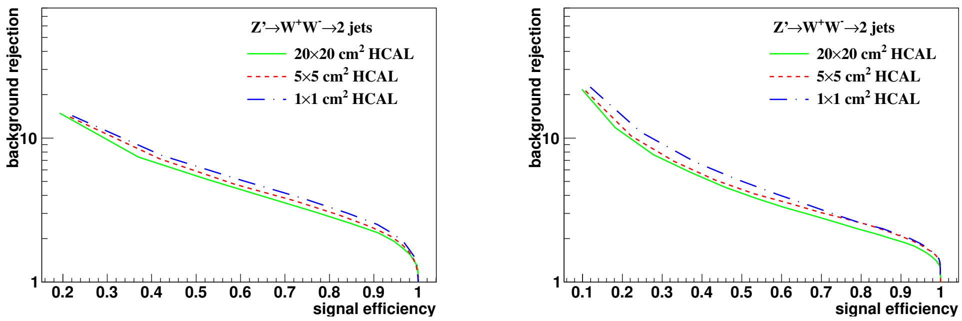

(a) Z' (5 TeV) (b) Z' (10 TeV)

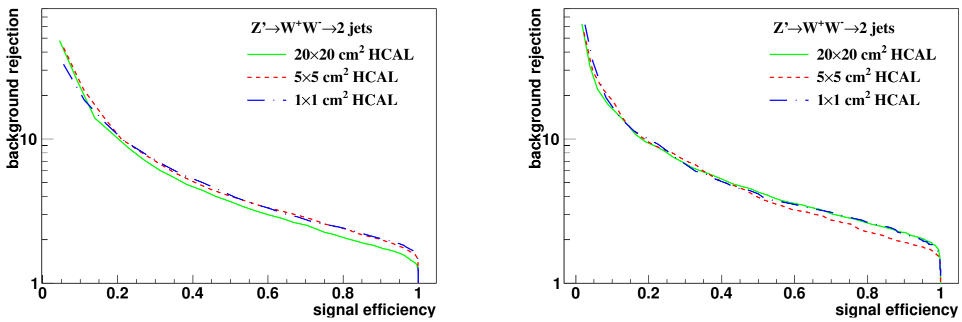

(c) Z' (20 TeV) (d) Z' (40 TeV)

Figure 8: The ROC curves of soft drop mass selection for β=2 with 5, 10, 20, 40 TeV c.m. energies. Three different detector cell sizes are compared: 20×20, 5×5, and 1×1 (cm^2). The signal (background) process is $Z' \to WW$ ($Z' \to q\bar{q}$).

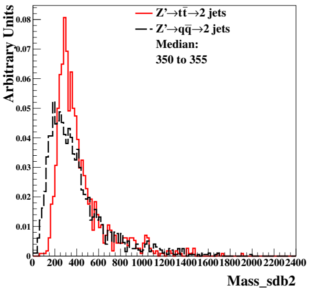

(a) 20×20 (cm^2)

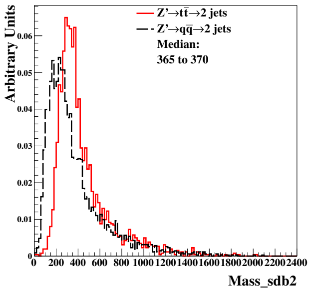

(b) 5×5 (cm^2)

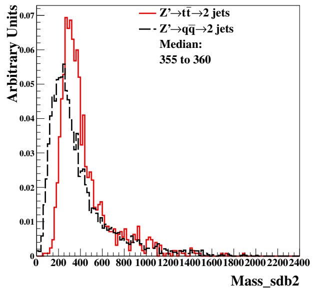

(c) 1×1 (cm^2)

Figure 9: Distributions of soft drop mass for β=2, with 20 TeV c.m. energies and three different detector cell sizes: 20×20, 5×5, and 1×1 (cm^2). The signal (background) process is $Z' \to t\bar{t}$ ($Z' \to q\bar{q}$).

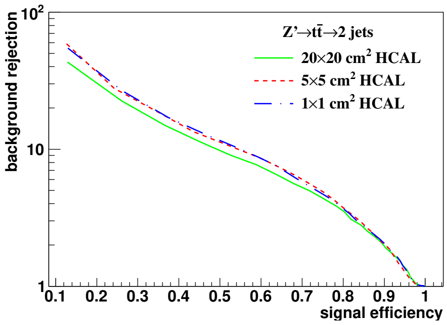

(a) Z'(5 TeV)

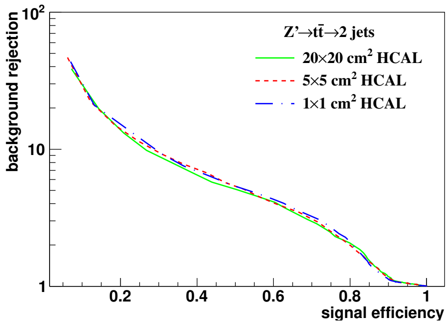

(b) Z'(10 TeV)

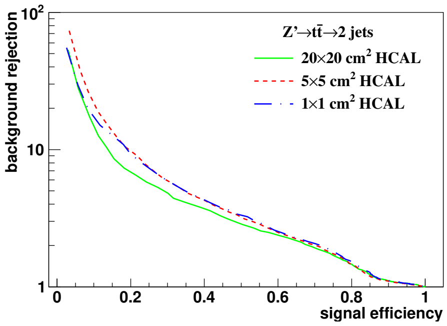

(c) Z'(20 TeV)

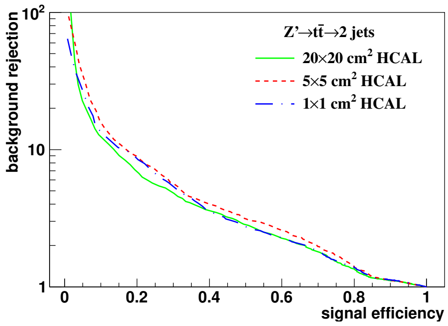

(d) Z'(40 TeV)

Figure 10: The ROC curves of soft drop mass selection for β=2 with 5, 10, 20, 40 TeV c.m. energies. Three different detector cell sizes are compared: 20×20, 5×5, and 1×1 (cm^2). The signal (background) process is $Z' \to t\bar{t}$ ($Z' \to q\bar{q}$).

5. Study of detector performance with jet substructure variables

In this section, we use several jet substructure variables to study the performance of detector with various detector cell sizes and c.m. energies.

5.1. N-subjettiness

The variable N-subjettiness [22], denoted by τ_N, is designed to "count" the number of subjet(s) in a large radius jet so to separate signal jets from decays of heavy bosons and background jets from QCD processes. The τ_N is the p_{T}-weighted angular distance between each jet constituent and the closest subjet axis:

$$\tau_N = \frac{1}{d_0} \sum_k p_{T,k} \mathrm{min}\{\Delta R_{1,k}, \Delta R_{2,k}, ...\Delta R_{N,k}\}, \tag{2}$$

with a normalization factor d_0:

$$d_0 = \sum_k p_{T,k} R_0.$$

The k runs over all constituent particles in a given large radius jet, $p_{T,k}$ is the transverse momentum of each individual constituent particle, $\Delta R_{j,k} = \sqrt{(\Delta y)^2 + (\Delta\phi)^2}$ is the distance between the constituent particle k and the candidate subjet axis j in the $y-\phi$ plane. The R_0 is the characteristic jet radius used in the anti-k_t jet algorithm.

In this analysis, the anti-k_t algorithm with $R = 0.4$ (AK4) is first employed to reconstruct jets. The subjet axes are obtained by running the exclusive k_t algorithm [23] and reversing the last N clustering steps. Namely, when τ_N is computed, the k_t algorithm is forced to return exactly N jets. If a large radius jet has N subjet(s), its τ_N is smaller than τ_{N-1}. Therefore, in our analysis, the ratio of the τ_N variables, τ_{21} (τ_2/τ_1) and τ_{32} (τ_3/τ_2), are used to distinguish the one-prong background jets and the two-prong jets from W or the three-prong jets from top.

We use the ROC curves as described in Section 4.2 to analyze the detector performance and determine the cell size that gives the best separation power to distinguish signal from background. Following the suggestion by Ref. [24], the requirement on the soft drop mass with $\beta = 0$ is applied before the study of N-subjettiness. For each detector configuration and c.m. energy, the soft drop mass selection is determined as follows. First, we look for the median bin of the soft drop mass histogram from simulated signal events as described in Section 4.2. Then, we compare the numbers of events in the bins adjacent to the medium bin (bin $i_{\mathrm{med}} - 1$ and bin $i_{\mathrm{med}} + 1$). The bin with larger number of events is added, in addition to the medium bin, to extend the mass window. The procedure is repeated until the window contains at least 75% of the total number of signal events.

In order to obtain the signal and background efficiencies, various ranges of τ_{21} and τ_{32} are scanned. Since some of the background distributions have long tails and leak into the signal-dominated region, we use the following method as suggested by the Pearson Lemma Method to determine the ranges of τ variables. First, we take the ratio of the signal to background τ_{21} (τ_{32}) histograms. The boundaries of the bin (seed bin) with maximum signal to background ratio (S/N) give us the first range of τ selection:

$x_{\rm low}^{\rm seedbin} < \tau_{21} < x_{\rm high}^{\rm seedbin}$. Then, we compare the S/N in the bins adjacent to the seed bin. The bin with larger S/N is added, in addition to the seed bin, to extend the τ_{21} selection window. Every window has its corresponding $\epsilon_{\rm sig}$ and $1/\epsilon_{\rm bkg}$ and an ROC curve is mapped out.

In addition to the ROC curves, we use the so-called "Mann-Whitney" test to quantify the detector performance. The value of Mann-Whitney is related to the integrated area under the ROC curve: if the value is bigger, it indicates the signal and background distributions have similar shapes and can not be well separated from each other. Vice versa, if the value is smaller, we can achieve a better signal and background separation.

Figures 11 and 13 show the distributions of τ_{21} and τ_{32} for $\sqrt{s} = 20$ TeV after applying the requirement on the soft drop mass. The signals considered are $Z' \rightarrow WW$ (τ_{21}) and $Z' \rightarrow t\bar{t}$ (τ_{32}). Figures 12 and 14 present the ROC curves from different detector cell sizes and c.m. energies, respectively. The smallest detector cell size (1×1 cm^2) does not have the best separation power. In fact, in some cases, the best separation power comes from a detector with bigger cell sizes (5×5 cm^2 and 20×20 cm^2).

Figures 17 (a) and (b) present the summary plots of τ_{21} and τ_{32} with various detector cell sizes and c.m. energies using Mann Whitney U test. For τ_{21} at smaller c.m. energies, when the cell size is smaller, the detector performance improves. However, when c.m. energy increases, no improvement is observed using the smallest detector cell size (1×1 cm^2). For τ_{32}, the case is similar to τ_{21}. It is interesting to note that at very large c.m. energies, the large detector cell sizes (5×5 cm^2 and 20×20 cm^2) have a better separation power than the smallest cell size considered in this analysis.

5.2. Energy correlation function

The energy correlation function (ECF) [25] is defined as follows:

$$ECF(N,\beta) = \sum_{i_1<i_2<....<i_N\in J} \left(\prod_{a=1}^{N} p_{\mathrm{T}ia}\right) \left(\prod_{b=1}^{N-1} \prod_{c=b+1}^{N} R_{i_b i_c}\right)^{\beta}, \tag{3}$$

where the sum is looped all particles in the jet J, $p_{\rm T}$ is the transverse momentum of each individual particle, and R is the distance between two particles in the y-ϕ plane. In order to use a dimensionless variable, a parameter r_N is defined:

$$r_N^{(\beta)} \equiv \frac{ECF(N+1,\beta)}{ECF(N,\beta)}. \tag{4}$$

The idea of r_N comes from N-subjettiness τ_N. Both r_N and τ_N are linear in the energy of the soft radiation for a system of N partons with soft radiation. In general, if the system has N subjets, $ECF(N+1,\beta)$ should be significantly smaller than $ECF(N,\beta)$. Therefore, we can use this feature to distinguish jets with different numbers of subjets. As in Section 5.1, the ratio r_N/r_{N-1}, denoted by C_N, (double ratios of ECFs) is used to study the detector performance:

$$C_N^{(\beta)} \equiv \frac{r_N^{(\beta)}}{r_{N-1}^{(\beta)}} = \frac{ECF(N-1,\beta)ECF(N+1,\beta)}{ECF(N,\beta)^2}. \tag{5}$$

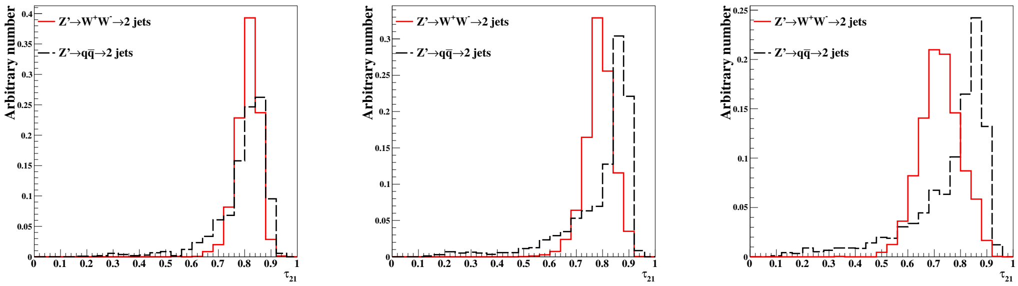

(a) 20×20 (cm^2) (b) 5×5 (cm^2) (c) 1×1 (cm^2)

Figure 11: Distributions of τ_{21} in 20 TeV energy collision for different detector sizes. Cell sizes in 20×20, 5×5, and 1×1 cm^2 are shown here.

In our analysis, we set $N = 2$ and $\beta = 1$ (C_2^1).

Figure 15 presents the histograms of C_2^1 with $\sqrt{s} = 20$ TeV after making the requirement on the soft drop mass. The signal considered is Z'→WW. Figure 16 shows the ROC curves from different detector cell sizes for each c.m. energy, respectively. One can see that the smallest detector cell size (1×1 cm^2) does not have the best signal/background separation power. Figure 17(c) summarizes the result of the Mann Whitney U test for C_2^1. When c.m. energy increases, no improvement is observed from detector with the smallest cell size.

6. Conclusions

The studies presented in this paper show that the reconstruction of jet substructure variables for future particle colliders will benefit from small cell sizes of the hadronic calorimeters. This conclusion was obtained using the realistic GEANT4simulation of calorimeter responses combined with reconstruction of calorimeter clusters used as inputs for jet reconstruction. Hadronic calorimeters that use the cell sizes of 20×20 cm^2 ($\Delta\eta \times \Delta\phi = 0.1 \times 0.1$) are least performat almost for every substructure variables considered in this analysis for jet transverse momenta between 2.5 to 10 TeV. Such cell sizes are close to those used for the ATLAS and CMS detectors at the LHC. In terms of the reconstruction of the physics-motivated quantities used for jet substructure studies, the performance of a hadronic callorimeter with $\Delta\eta \times \Delta\phi = 0.022 \times 0.022$ is, in most cases, better than for a detector with 0.1×0.1 cells. Thus this study confirms the baseline SiFCC detector geometry [7] that uses $\Delta\eta \times \Delta\phi = 0.022 \times 0.022$ HCAL cells. The performance of the HCAL with cells $\Delta\eta \times \Delta\phi = 0.01 \times 0.01$ and $\Delta\eta \times \Delta\phi = 0.005 \times 0.005$ were found to be similar.

It interesting to note that, for very boosted jets with transverse momenta close to 20 TeV, no significant improvement with the decrease of cell sizes was observed. This result needs to be understood in terms of various type of simulations and different options for construction of the calorimeter clusters.

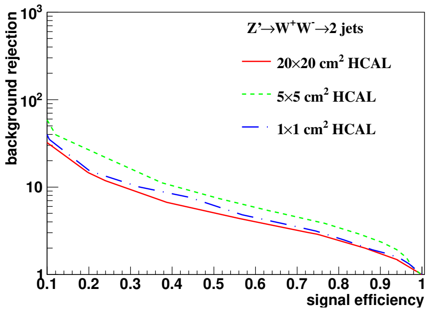

(a) Z'(5 TeV)

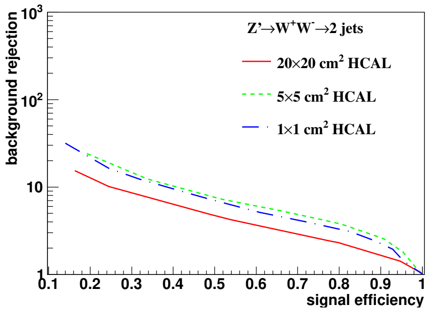

(b) Z'(10 TeV)

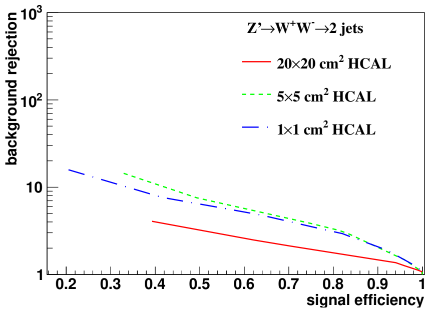

(c) Z'(20 TeV)

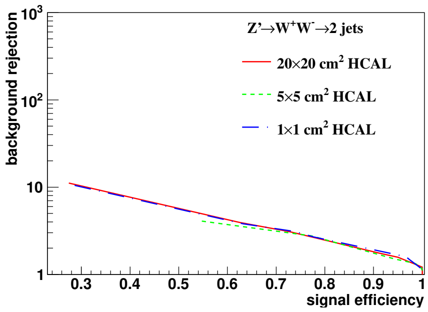

(d) Z'(40 TeV)

Figure 12: Signal efficiency versus background rejection rate using τ_{21}. The energies of collision at (a) 5, (b) 10, (c) 20, and (d) 40 TeV are shown here. In each figure, the three ROC curves correspond to different detector sizes.

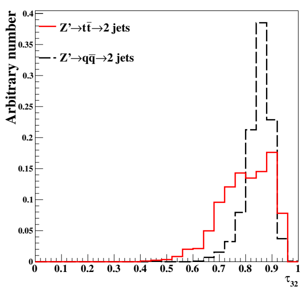

(a) 20×20 (cm^2)

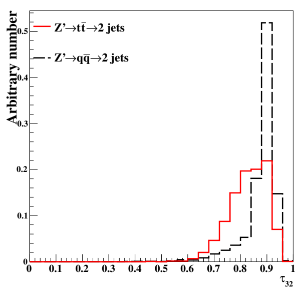

(b) 5×5 (cm^2)

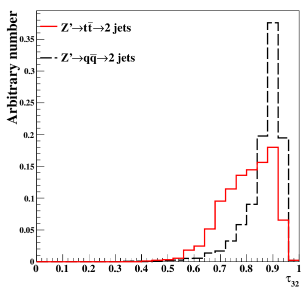

(c) 1×1 (cm^2)

Figure 13: Distributions of τ_{32} in 20 TeV energy collision for different detector sizes. Cell sizes in 20×20, 5×5, and 1×1 cm^2 are shown here.

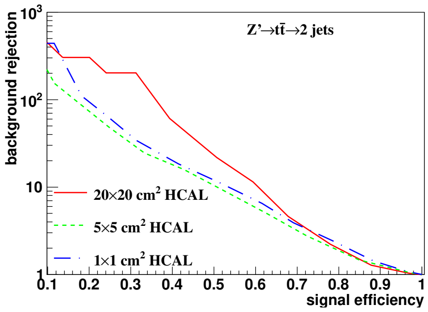

(a) Z'(5 TeV)

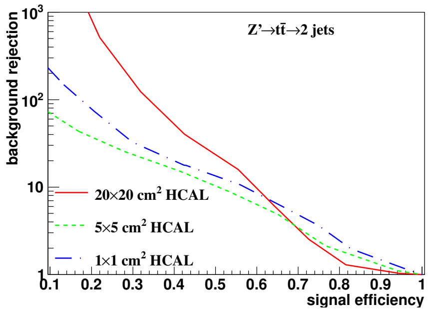

(b) Z'(10 TeV)

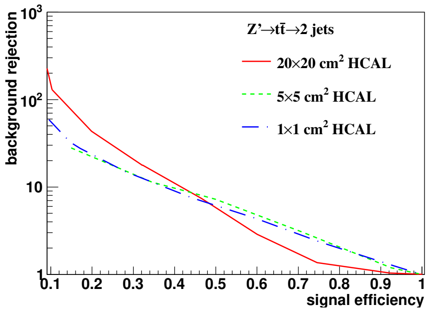

(c) Z'(20 TeV)

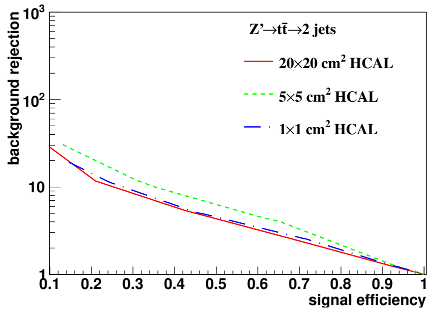

(d) Z'(40 TeV)

Figure 14: Signal efficiency versus background rejection rate using τ_{32}. The energies of collision at (a) 5, (b) 10, (c) 20, and (d) 40 TeV are shown here. In each figure, the three ROC curves correspond to different detector sizes.

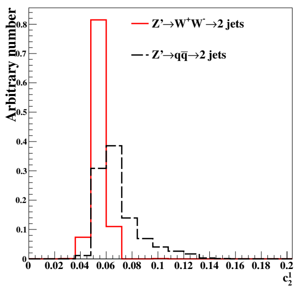

(a) 20×20 (cm^2)

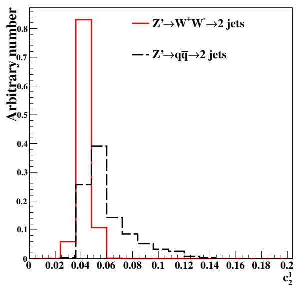

(b) 5×5 (cm^2)

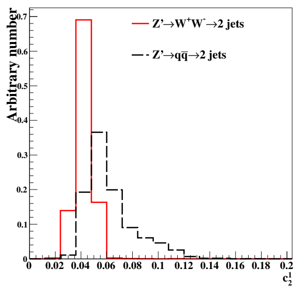

(c) 1×1 (cm^2)

Figure 15: Distributions of C_2^1 in 20 TeV energy collision for different detector sizes. Cell sizes in 20×20, 5×5, and 1×1 cm^2 are shown here.

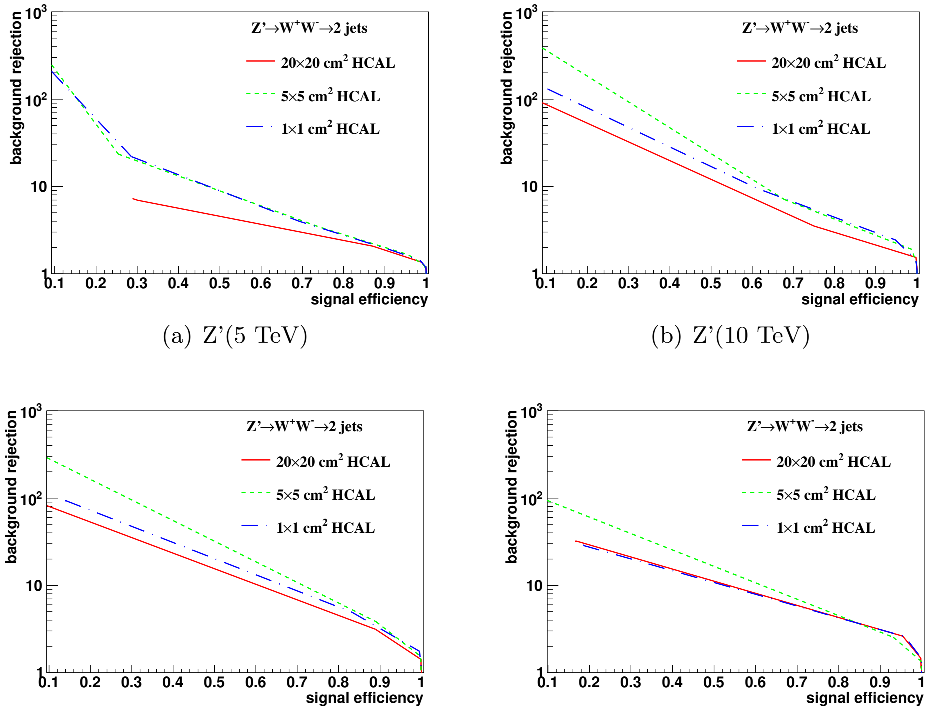

(a) Z'(5 TeV) (b) Z'(10 TeV)

(c) Z'(20 TeV) (d) Z'(40 TeV)

Figure 16: Signal efficiency versus background rejection rate using C_2^1. The energies of collision at (a) 5, (b) 10, (c) 20, and (d) 40 TeV are shown here. In each figure, the three ROC curves correspond to different detector sizes.

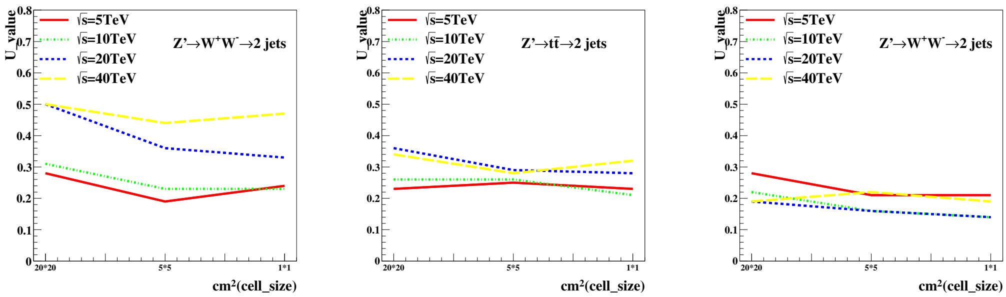

(a) τ_{21} (b) τ_{32} (c) $C_2^{(1)}$

Figure 17: The Mann-Whitney U values for τ_{21}, τ_{32}, and $C_2^{(1)}$ reconstructed with different collision energies and detector cell sizes.

Acknowledgements

This research was performed using resources provided by the Open Science Grid, which is supported by the National Science Foundation and the U.S. Department of Energy's Office of Science. We gratefully acknowledge the computing resources provided on Blues , a high-performance computing cluster operated by the Laboratory Computing Resource Center at Argonne National Laboratory. Argonne National Laboratory's work was supported by the U.S. Department of Energy, Office of Science under contract DE-AC02-06CH11357. The Fermi National Accelerator Laboratory (Fermilab) is operated by Fermi Research Alliance, LLC under Contract No. DE-AC02-07CH11359 with the United States Department of Energy.

References

[1] M. Benedikt, The Global Future Circular Colliders EffortCERN-ACC-SLIDES-2016-0016. Presented at P5 Workshop on the Future of High Energy Physics, BNL, USA, Dec. 15-18, 2013. URL http://cds.cern.ch/record/2206376

[2] J. Tang, et al., Concept for a Future Super Proton-Proton Collider (2015). arXiv:1507.03224.

[3] R. Calkins, et al., Reconstructing top quarks at the upgraded LHC and at future accelerators, in: Proceedings, Community Summer Study 2013: Snowmass on the Mississippi (CSS2013): Minneapolis, MN, USA, July 29-August 6, 2013. arXiv:1307.6908. URL https://inspirehep.net/record/1244676/files/arXiv:1307.6908.pdf

[4] S. V. Chekanov, J. Dull, Energy range of hadronic calorimeter towers and cells for high-pT jets at a 100 TeV colliderarXiv:1511.01468.

[5] E. Coleman, M. Freytsis, A. Hinzmann, M. Narain, J. Thaler, N. Tran, C. Vernieri, The importance of calorimetry for highly-boosted jet substructurearXiv:1709.08705.

[6] DELPHES 3 Collaboration, J. de Favereau, C. Delaere, P. Demin, A. Giammanco, V. Lematre, A. Mertens, M. Selvaggi, DELPHES 3, A modular framework for fast simulation of a generic collider experiment, JHEP 02 (2014) 057. arXiv:1307.6346, doi:10.1007/JHEP02(2014)057.

[7] S. V. Chekanov, M. Beydler, A. V. Kotwal, L. Gray, S. Sen, N. V. Tran, S. S. Yu, J. Zuzelski, Initial performance studies of a general-purpose detector for multi-TeV physics at a 100 TeV pp collider, JINST 12 (06) (2017) P06009. arXiv:1612.07291, doi:10.1088/1748-0221/12/06/P06009.

[8] J. Allison, et al., Recent developments in Geant4, Nuclear Instruments and Methods in Physics Research A 835 (2016) 186.

[9] M. J. Charles, PFA Performance for SiD, in: Linear colliders. Proceedings, International Linear Collider Workshop, LCWS08, and International Linear Collider Meeting, ILC08, Chicago, USA, Novermber 16-20, 2008 , 2009. arXiv:0901.4670.

[10] J. S. Marshall, M. A. Thomson, Pandora Particle Flow Algorithm, in: Proceedings, International Conference on Calorimetry for the High Energy Frontier (CHEF 2013), 2013, pp. 305–315. arXiv:1308.4537.

[11] G. P. S. M. Cacciari, G. Soyez, FastJet user manual CERN-PH-TH/2011-297. arXiv:1111.6097.

[12] M. Cacciari, G. P. Salam, G. Soyez, The anti-kt jet clustering algorithm, JHEP 0804 (2008) 063. arXiv:0802.1189.

[13] S. Chekanov, HepSim: a repository with predictions for high-energy physics experiments, Advances in High Energy Physics 2015 (2015) 136093, available as http://atlaswww.hep.anl.gov/hepsim/.

[14] B. Auerbach, S. Chekanov, J. Love, J. Proudfoot, A. Kotwal, Sensitivity to new high-mass states decaying to ttbar at a 100 TeV collider arXiv:1412.5951.

[15] J. Butterworth, B. Cox, J. R. Forshaw, WW scattering at the CERN LHC, Phys.Rev. D65 (2002) 096014. arXiv:hep-ph/0201098, doi:10.1103/PhysRevD.65.096014.

[16] S. Catani, Y. L. Dokshitzer, M. H. Seymour, B. R. Webber, Longitudinally-invariant k-clustering algorithms for hadron-hadron collisions, Nuclear Physics B 406 (12) (1993) 187 – 224. URL http://www.sciencedirect.com/science/article/pii/055032139390166M

[17] S. D. Ellis, D. E. Soper, Successive combination jet algorithm for hadron collisions, Phys. Rev. D48 (1993) 3160–3166. arXiv:hep-ph/9305266, doi:10.1103/PhysRevD.48.3160.

[18] ATLAS Collaboration Collaboration, G. Aad, et al., Jet mass and substructure of inclusive jets in $\sqrt{s} = 7$ TeV pp collisions with the ATLAS experiment, JHEP 1205 (2012) 128. arXiv:1203.4606, doi:10.1007/JHEP05(2012)128.

[19] A. J. Larkoski, S. Marzani, G. Soyez, J. Thaler, Soft Drop, JHEP 05 (2014) 146. arXiv:1402.2657, doi:10.1007/JHEP05(2014)146.

[20] Y. L. Dokshitzer, G. D. Leder, S. Moretti, B. R. Webber, Better jet clustering algorithms, JHEP 08 (1997) 001. arXiv:hep-ph/9707323, doi:10.1088/1126-6708/1997/08/001.

[21] M. Wobisch, T. Wengler, Hadronization corrections to jet cross-sections in deep inelastic scattering, in: Monte Carlo generators for HERA physics. Proceedings, Workshop, Hamburg, Germany, 1998-1999, 1998, pp. 270–279. arXiv:hep-ph/9907280.

[22] J. Thaler, K. Van Tilburg, Identifying Boosted Objects with N-subjettiness, JHEP 03 (2011) 015. arXiv:1011.2268, doi:10.1007/JHEP03(2011)015.

[23] S. Catani, Y. L. Dokshitzer, M. H. Seymour, B. R. Webber, Longitudinally-invariant $k_\perp$-clustering algorithms for hadron-hadron collisions, Nucl. Phys. B 406 (CERN-TH-6775-93. LU-TP-93-2) (1993) 187–224.

[24] F. A. Dreyer, L. Necib, G. Soyez, J. Thaler, Recursive Soft Drop, JHEP 06 (2018) 093. arXiv:1804.03657, doi:10.1007/JHEP06(2018)093.
[25] A. J. Larkoski, G. P. Salam, J. Thaler, Energy Correlation Functions for Jet Substructure, JHEP 06 (2013) 108. arXiv:1305.0007, doi:10.1007/JHEP06(2013)108.